

# Real-Time Indoor Object SLAM with LLM-Enhanced Priors

Yang Jiao<sup>1</sup>, Yiding Qiu<sup>1</sup> and Henrik I. Christensen<sup>2</sup>

**Abstract**—Object-level Simultaneous Localization and Mapping (SLAM), which incorporates semantic information for high-level scene understanding, faces challenges of under-constrained optimization due to sparse observations. Prior work has introduced additional constraints using commonsense knowledge, but obtaining such priors has traditionally been labor-intensive and lacks generalizability across diverse object categories. We address this limitation by leveraging large language models (LLMs) to provide commonsense knowledge of object geometric attributes, specifically size and orientation, as prior factors in a graph-based SLAM framework. These priors are particularly beneficial during the initial phase when object observations are limited. We implement a complete pipeline integrating these priors, achieving robust data association on sparse object-level features and enabling real-time object SLAM. Our system, evaluated on the TUM RGB-D and 3RScan datasets, improves mapping accuracy by 36.8% over the latest baseline. Additionally, we present real-world experiments in the supplementary video, demonstrating its real-time performance.

## I. INTRODUCTION

Object Simultaneous Localization and Mapping (SLAM) builds environment maps by identifying and localizing objects, and using this information to infer the robot's position. Unlike traditional feature-based SLAM, object-level representations are sparse, focusing on semantic object data. Comparing to semantic segmentation on dense representations, such sparsity improves computational efficiency and reduces storage requirements. Meanwhile, high-level semantic information makes object SLAM useful for downstream tasks, such as 3D semantic scene reconstruction, object-goal navigation, and object retrieval [1].

When navigating an unfamiliar environment to find specific objects, the agent must efficiently build a map while moving quickly to cover large areas, often resulting in limited observations of objects from different viewpoints [2]. SLAM with sparse observations commonly occurred in real-world applications, such as when the camera frame rate is low relative to the agent's motion speed or when loop closure is unavailable. However, due to the inherent sparsity of object-level features, fewer-constraint object SLAM can be extremely challenging. Such sparsity affects the quality of initial mapping and might hinder subsequent optimization and data association.

To address these issues, we introduce additional constraints from commonsense knowledge. Objects typically exhibit common attributes, such as size, shape, and orientation,

<sup>1</sup>Students of Contextual Robotics Institute, University of California San Diego, La Jolla, CA 92093, USA {y4jiao, yiqiu}@ucsd.edu

<sup>2</sup>Henrik I. Christensen is with Faculty of the Department of Computer Science and Engineering, University of California San Diego, La Jolla, CA 92093, USA hichristensen@ucsd.edu



Fig. 1: An overview of our object SLAM. We utilized prior knowledge of the objects from LLM and achieved a robust real-time object SLAM system. This approach enables the construction of a semantically meaningful, object-level map.

which provide valuable priors for mapping systems. These attributes are essential during the initial observation phase, where limited 2D features and uncertain pose estimations bring challenges. By incorporating these priors, the solution space for object estimation can be effectively constrained, enhancing mapping accuracy in sparse observation scenarios. However, acquiring comprehensive object priors has traditionally been labor-intensive, requiring substantial human annotation across diverse object categories [3]. Furthermore, commonsense knowledge about objects can vary by context, leading to potential mismatches between expected and actual observations.

We leveraged large language models (LLMs) to provide prior information, as commonsense inference is LLM's strong suit [4]. We propose a LLM-enhanced prior-assisted object SLAM framework to address the challenge of under-constrained optimization in object SLAM. Our approach models the prior knowledge from LLM as factors using a factor graph [5]. Specifically, we focus on the geometric intrinsics of size and orientation for various object categories.

Our method integrates prior information from LLM and a combined data association method to achieve a full online object SLAM (Fig. 1). We validated it on real-world datasets. The key contributions of this paper are outlined below:

- Exploration of using commonsense priors, particularly object size and orientation, and encoding them as prior factors for a graph-based SLAM system;
- A complete pipeline from embedding LLM-enhanced priors, extracting object-level features, performing data association, to solving incremental optimization;
- Evaluation using two real-world datasets: TUM RGB-D and 3RScan, and test of our SLAM method in real-time.

## II. RELATED WORK

### A. Object-level semantic SLAM

Semantic SLAM has evolved from treating semantic information as an “add-on” to metric maps to integrating object constraints in trajectory optimization. While some approaches require dense point clouds [6] or CAD models [7], generalized geometric representations have emerged for simplicity. The field predominantly uses two forms: quadric forms (ellipsoids) as in QuadricSLAM [8] and cube forms as in CubeSLAM [9]. CubeSLAM provides stronger constraints with rectangular 3D bounding boxes but struggles with irregularly shaped objects, while QuadricSLAM is more versatile for general object-level semantic SLAM.

Several works have built upon the QuadricSLAM approach [1], [10]–[12], each with different emphases. The original QuadricSLAM required human-labeled data associations and solved through batch optimization. Qian et al. [13] employed dense object keypoint features for automatic data association but did not focus on improving mapping quality. SO-SLAM [11] emphasized first-frame initialization of objects and demonstrated the utility of spatial constraints. They evaluated their mapping techniques for initialization and used bundle adjustment with ground-truth data association for entire scenes. In contrast, our approach is tailored for real-time full-SLAM processing with online data association. EAO-SLAM [10] represents a similar work that adopts the CubeSLAM approach with line segmentation as joint localization methods, transforming cubes into quadric representations to map specific object classes. Meanwhile, EAO-SLAM also resolves data association via statistics test on dense visual features. More recently, VOOM [12] improved upon OA-SLAM [14] by employing a hierarchical coarse-to-fine approach that combines dual quadrics for object representation with enhanced feature point data association, demonstrating superior localization performance. Since both EAO-SLAM and VOOM optimize mapping with online data association, we compare our model with these systems in our experimental evaluation.

### B. Semantic methods with prior knowledge

In robotics, prior knowledge is helpful across various disciplines [15], [16]. Within the specific context of object-based SLAM, a follow-up work from QuadricSLAM authors attempted to use orientation [3] and then plane structures [17] as constraints. Similarly, SO-SLAM [11] leverages object-plane contact, object relative scales, and symmetry properties, showing an improved performance in initializing objects in SLAM. The key idea of our proposed method is to use prior factors not only for the initialization but throughout the optimization process because the constraints are useful in the incremental setting, especially when using geometric features in online data association.

As LLMs have grown in capability and prominence, the robotics research community has increasingly leveraged their potential. Recent work has applied LLMs to various domains, including indoor object navigation [18], functional

object search [4], and tasks planning [19]. Studies [20] have demonstrated that LLMs encode significant commonsense knowledge about physical objects and their properties. To the best of our knowledge, our work presents the first attempt to incorporate generalized object knowledge from LLMs directly into SLAM systems, bridging the gap between high-level semantic representations and geometric mapping.

## III. METHODOLOGY

Fig. 2 presents an overview of our object SLAM system. The odometry is estimated by tracking visual features from an RGB-D camera. Meanwhile, our system detects the per-frame 2D object features and performs inter-frame object tracking (short-term), and map-to-image object association (long-term). The object SLAM module, utilizing a factor graph approach [5], takes the estimated odometry and the associated object observations as input. LLM is leveraged to generate commonsense priors for objects based on the vocabulary of the object detector, where the priors are modeled as unary factors in the factor graph (Fig. 3). Finally, an incremental optimizer, such as iSAM2 [21], updates the object map and the odometry.

### A. Object SLAM problem

The object SLAM problem is set up with a sequence of camera poses  $\mathcal{X} = \{\mathbf{x}_i \in SE(3) | i \in \{1, \dots, M\}\}$  and the object landmarks,  $\mathcal{Q} = \{\mathbf{q}_j \in \mathbb{R}^9 | j \in \{1, \dots, N\}\}$ . The odometry measurements,  $\mathcal{U} = \{\mathbf{u}_i \in SE(3) | i \in \{1, \dots, M-1\}\}$ , represent the estimated pose transformation between two consecutive camera poses,  $\mathbf{x}_{i+1} = f(\mathbf{x}_i, \mathbf{u}_i) + \mathbf{w}_i$ . The motion model  $f(\cdot)$  is simply  $f(\mathbf{x}_i, \mathbf{u}_i) = \mathbf{x}_i \oplus \mathbf{u}_i$ , where the  $\oplus$  operator denotes the summation operation over  $SE(3)$ .  $\mathbf{w}_i$  is the Gaussian white noise with covariance  $\Sigma_f$ , i.e.,  $\mathbf{w}_i \sim \mathcal{N}(\mathbf{0}, \Sigma_f)$ .

For the object landmarks, we follow the formulation as in QuadricSLAM [8], where ellipsoids represent all landmarks.  $\mathbf{q}_j$  characterizes the 9 degrees of freedom (DoFs) for a quadric, i.e., the rotation angles  $\boldsymbol{\theta} = (\theta_x, \theta_y, \theta_z)^T$ , the quadric centroid translation  $\mathbf{t} = (t_x, t_y, t_z)^T$ , and the lengths of 3 semi-axes  $\mathbf{s} = (s_x, s_y, s_z)^T$ , where  $\mathbf{q} = (\boldsymbol{\theta}^T, \mathbf{t}^T, \mathbf{s}^T)^T$ . The object landmarks are observed as on-image bounding boxes using visual object detectors such as the YOLO [22]. The object observations are denoted as  $\mathcal{B} = \{\mathbf{b}_{ik} \in \mathbb{R}^4 | k \in \{1, \dots, L_i\}\}$  where  $L_i$  is the number of observed objects in the  $i$ -th frame,  $\mathbf{b}_{ik}$  represents the  $k$ -th bounding box in the  $i$ -th frame. Each bounding box is represented as  $\mathbf{b} = (x_{\min}, y_{\min}, x_{\max}, y_{\max})^T$ . Given  $\mathbf{x}_i$  and  $\mathbf{q}_j$ , a predicted bounding box  $\hat{\mathbf{b}}$  is obtained by projecting  $\mathbf{q}_j$  onto the image plane. The observation model is denoted as  $\mathbf{b}_{ij} = \boldsymbol{\beta}(\mathbf{x}_i, \mathbf{q}_j)$ , where implementation is detailed in [8].

We denote the prior and initial measurements of each quadric as  $\boldsymbol{\alpha}_j$ , and  $\mathcal{A} = \{\boldsymbol{\alpha}_j | j \in \{1, \dots, N\}\}$ . The probability distribution over all camera poses and quadric landmarks can be factorized as:

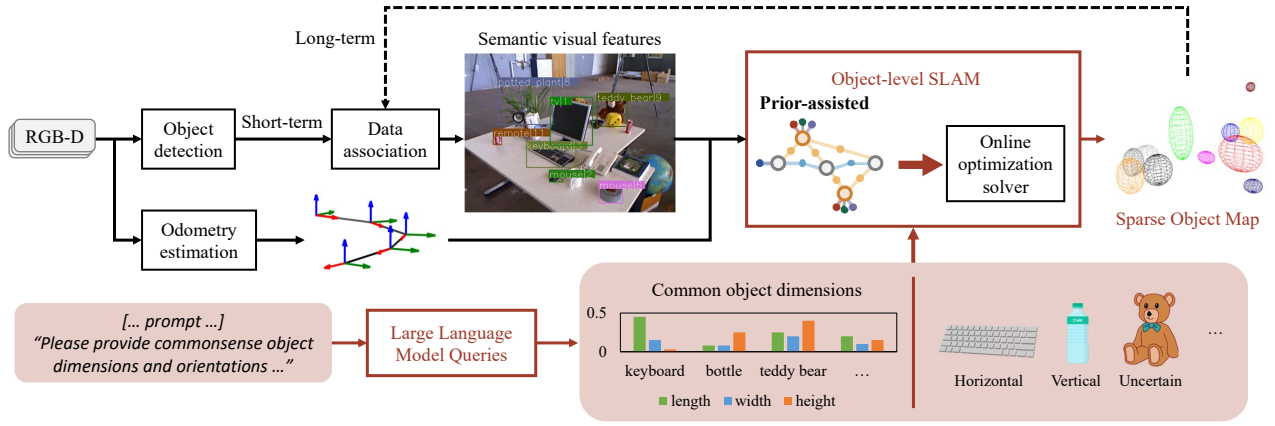


Fig. 2: The pipeline of our object SLAM method. We describe our SLAM system by showing the usage of LLM and the data flow from a sequence of image frames to the object-level map. Our main contributions are highlighted in red.

$$\begin{aligned}
 P(\mathcal{X}, \mathcal{Q} | \mathcal{U}, \mathcal{B}, \mathcal{A}) &\propto \prod_i P(\mathbf{x}_{i+1} | \mathbf{x}_i, \mathbf{u}_i) \\
 &\cdot \prod_{ij} P(\mathbf{q}_j | \mathbf{x}_i, \mathbf{b}_{ij}) \cdot \prod_j P(\mathbf{q}_j | \boldsymbol{\alpha}_j)
 \end{aligned} \tag{1}$$

We can then formulate the maximum a posteriori (MAP) problem by maximizing the joint probability in (1):

$$\begin{aligned}
 \mathcal{X}^*, \mathcal{Q}^* &= \underset{\mathcal{X}, \mathcal{Q}}{\operatorname{argmin}} -\log P(\mathcal{X}, \mathcal{Q} | \mathcal{U}, \mathcal{B}, \mathcal{A}) \\
 &= \underset{\mathcal{X}, \mathcal{Q}}{\operatorname{argmin}} \sum_i \|f(\mathbf{x}_i, \mathbf{u}_i) \ominus \mathbf{x}_{i+1}\|_{\Sigma_f}^2 \\
 &\quad + \sum_{ij} \|\mathbf{b}_{ij} - \boldsymbol{\beta}(\mathbf{x}_i, \mathbf{q}_j)\|_{\Lambda_{ij}}^2 \\
 &\quad + \sum_j \|g(\mathbf{q}_j) - \boldsymbol{\alpha}_j\|_{\Sigma_\alpha}^2
 \end{aligned} \tag{2}$$

where the  $\ominus$  operator denotes the difference operation in SE(3),  $\|\mathbf{a} - \mathbf{b}\|_{\Sigma}$  is the Mahalanobis distance with covariance matrix  $\Sigma$ , and  $g(\cdot)$  represents a general transform function on the quadric  $\mathbf{q}_j$  such that  $g(\mathbf{q}_j)$  can be directly compared with the prior estimates.

### B. Factor graph and LLM-enhanced priors

With the MAP problem setup, we can utilize factor graphs to characterize the object-level SLAM efficiently. Fig. 3 shows a toy example of the factor graph structure with our commonsense prior factors. We introduce the size and orientation priors, deriving from commonsense knowledge using LLM. Besides, we designed a unary factor with initial object centroid measurement, drawing from a single-frame RGB-D observation of objects, to facilitate fewer-frame object SLAM optimization.

1) *Size prior*: Human language mostly describes the size of an object using length, width, and height, while axis lengths most easily describe the size of ellipsoids. We use LLM to generate the length, width, and height for a list of object categories. However, an object can have different

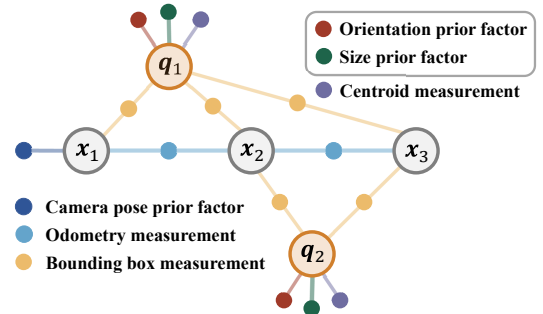


Fig. 3: A toy example to show the factor graph structure in our object SLAM. Object orientation and size prior factors are encoded with commonsense knowledge from LLM.

rotations, and a fixed correspondence between axis lengths and length, width, and height is not guaranteed. Therefore, we re-ordered the landmark size measurements to determine the dissimilarity between the axis length estimation and the size prior. The re-ordering operation is denoted by a permutation matrix  $P_s$ , such that  $\hat{s} = P_s s$ , where  $\hat{s}$  contains all entries in  $s$  in ascending order. For a given commonsense size of an object  $s_r$  in the format of length-width-height, the respective prior estimate of size is  $s_\alpha = P_s s_r / 2$ . We divide  $s_r$  by 2 to be consistent with the representations of the semi-axis length for a quadric.

In practice, we found that the effectiveness of the size prior is highly dependent on the accuracy of the object label, which is provided by the object detector. Hence, we combined  $s_\alpha$  with the initial size of the quadric  $s_o$ , which is derived from the initial bounding box dimensions and the depth estimation within the bounding box. We formulated the prior estimate as  $\hat{s}_\alpha = p \cdot s_\alpha + (1 - p)s_o$ , where  $p \in [0, 1]$  is the confidence score for the object observation given by the object detector. Note that state-of-the-art object detection algorithms can have high confidence score even for partially observed objects, and thus our size prior is necessary to correct such occluded observations.

2) *Orientation prior*: The fundamental rule for orientation prior factors incorporates that the rotation of real-world objects is aligned with gravity. Moreover, based on the

affordance of objects, an object can have (1) vertical, (2) horizontal, or (3) uncertain orientation. Vertical objects have a height greater than their length and width, i.e., the object size along the z-axis is larger than their x- and y-axes. For instance, bottles and chairs are normally upright because of their designed functions and usually have height as the longest dimension. On the other hand, horizontal objects, such as keyboards and plates, have a height significantly smaller than their length and width. Under the uncertain orientation category, objects can either be common to manipulate into various rotations (e.g., books and teddy bears) or have all three dimensions in similar lengths (e.g., balls and bowls). The rotation of the ellipsoid representation of the latter ones is not interesting for optimization since the shape of the ellipsoid will be very close to a sphere, and we simply follow the base rule of the gravity constraint.

For vertical objects, we align the longest semi-axis of the quadric with the z-axis of the world frame,  $\mathbf{w}_z = [0, 0, 1]^T$ , where the semi-axis lengths are obtained from initial observation  $\mathbf{s}_o$ . The longest axis of the horizontal objects is projected to the world x-y plane.

For uncertain objects, we perform gravity alignment with minimum projection error. Denote the initial quadric orientation using rotation matrix  $R_q = [\mathbf{r}_x, \mathbf{r}_y, \mathbf{r}_z]$ , and the gravity-aligned quadric rotation  $\hat{R}_q = [\hat{\mathbf{r}}_x, \hat{\mathbf{r}}_y, \mathbf{w}_z]$ . We set  $\hat{\mathbf{r}} = \operatorname{argmin}_{\mathbf{r} \in (\mathbf{r}_x, \mathbf{r}_y, \mathbf{r}_z)} |\mathbf{r}^T \mathbf{w}_z|$ , and hence  $\hat{\mathbf{r}}$  is the initial rotation axis closest to the world x-y plane. The orthogonal projection of  $\hat{\mathbf{r}}$  onto the world x-y plane gives the minimum projection error in  $L_2$ -norm while revising the quadric orientation to be aligned with gravity. We estimate  $\hat{\mathbf{r}}_y$  by a Gram-Schmidt step, i.e.,  $\hat{\mathbf{r}}_y = \frac{\hat{\mathbf{r}} - (\hat{\mathbf{r}}^T \mathbf{w}_z) \mathbf{w}_z}{\|\hat{\mathbf{r}} - (\hat{\mathbf{r}}^T \mathbf{w}_z) \mathbf{w}_z\|_2}$ , where  $\hat{\mathbf{r}}_y$  defines the gravity-aligned y-axis of the quadric.  $\hat{\mathbf{r}}_x$  can be recovered by  $\hat{\mathbf{r}}_x = \hat{\mathbf{r}}_y \times \mathbf{w}_z$ .

3) *Centroid factor*: For the centroid factor, we encode the initial guess of the object centroid  $\mathbf{t}_\alpha$  as a unary factor. We utilize the depth image to obtain the initial guess of the object’s centroid location. The centroid factor is used to constrain the position of a quadric, especially in the case of occlusion.

4) *Cost function and variance settings*: We denote the cost term for prior factor and initial measurement in (2) as  $e_\alpha^{(j)} := \|g(\mathbf{q}_j) - \alpha_j\|_{\Sigma_\alpha^{(j)}}^2$ . For any landmark  $\mathbf{q}$ :

$$e_\alpha = \|\boldsymbol{\theta} - \boldsymbol{\theta}_\alpha\|_{\Sigma_\theta}^2 + \|\mathbf{t} - \mathbf{t}_\alpha\|_{\Sigma_t}^2 + \|P_s \mathbf{s} - \mathbf{s}_\alpha\|_{\Sigma_s}^2 \quad (3)$$

where the joint covariance matrix  $\Sigma_\alpha = \operatorname{diag}(\Sigma_\theta, \Sigma_t, \Sigma_s)$ , the transform function  $g(\mathbf{q}) = (\boldsymbol{\theta}^T, \mathbf{t}^T, P_s \mathbf{s}^T)^T$ , and  $\boldsymbol{\alpha} = (\boldsymbol{\theta}_\alpha^T, \mathbf{t}_\alpha^T, \mathbf{s}_\alpha^T)^T$ .

In terms of covariance setting, we set  $\Sigma_\theta = \operatorname{diag}(k_x^2, k_y^2, k_z^2)$  with  $k_x, k_y \in (0, \frac{\pi}{16})$  and  $k_z \in (\frac{\pi}{2}, \pi)$ . We also set  $\Sigma_t$  and  $\Sigma_s$  such that the standard deviation is proportional to the inquired object size, i.e.,  $\Sigma_t = k_t^2 \cdot \operatorname{diag}(\mathbf{s}_\alpha)^2$  and  $\Sigma_s = k_s^2 \cdot \operatorname{diag}(\mathbf{s}_\alpha)^2$ .  $k_t$  and  $k_s$  are set in the range of (0.5, 2).

### C. Object association

The object-level data association is implemented by coordinating on-image object tracking (e.g., SORT [23] and its

variations [24], [25]) and the matching between landmarks and bounding boxes for long-term association. The long-term data association task is modeled as a linear sum assignment problem (LSAP). Specifically, LSAP finds the bijection between all  $\mathbf{b}_i$  and  $\mathbf{q}$ , such that the summation of weights  $w_{kj}^{(i)} := w(\mathbf{b}_{ik}, \mathbf{q}_j)$  over all pairs of  $\mathbf{b}_{ik}$  and  $\mathbf{q}_j$  can be maximized.

Define a weight matrix  $W^{(i)} = (w_{kj}^{(i)})$  for data association:

$$w_{kj}^{(i)} = \operatorname{IoU}(\mathbf{b}_{ik}, \beta(\mathbf{x}_i, \mathbf{q}_j)) + w_s \cdot \psi_{kj}^{(i)} + w_d \cdot \frac{1}{\|\mathbf{t}_j - \hat{\mathbf{t}}_{ik}\|_2} \quad (4)$$

where IoU represents Intersection-over-Union,  $w_s$  is a constant semantic weight, and  $\psi_{kj}^{(i)}$  is defined as:

$$\psi_{kj}^{(i)} = \begin{cases} 1 & \text{if } \|\mathbf{v}_{ik}^b - \mathbf{v}_j^q\|_2 \leq s_{th} \\ 0 & \text{otherwise} \end{cases} \quad (5)$$

where  $\mathbf{v}$  is the GloVe word embedding [26] for the class label of a bounding-box detection  $\mathbf{b}_{ik}$  or a landmark  $\mathbf{q}_j$ , and  $s_{th}$  is a semantic threshold. In this case, a higher association weight is assigned to the detection and landmark with similar class labels.  $\hat{\mathbf{t}}_{ik}$  represents the reprojected centroid from a bounding box observation to a 3D point in the world frame. The reprojection procedure adopts the depth image information and uses the same method as obtaining the centroid factor estimation.  $w_d$  is a hyperparameter for scaling. The last term in (4), which is inversely proportional to the distance between an ellipsoid centroid and a reprojected centroid, identifies data association when an object has a relatively small size and is hard to track using IoU. Combining the weights of IoU, semantic matching, and distance, we have the weight function for LSAP as  $w(\mathbf{b}_{ik}, \mathbf{q}_j) = w_{kj}^{(i)}$ , where solving the LSAP yields the long-term object-level association.

### D. Generating Object Priors using Large Language Models

We use LLMs to generate commonsense object priors, specifically size dimensions and orientation information, to enhance object-level SLAM performance. Our implementation used Claude 3.7 Sonnet. The methodology is also generalizable to other LLM architectures with sufficient semantic knowledge.

LLMs encode substantial commonsense knowledge about the physical world through their training on vast text corpora. We exploit this capability to extract structured information about everyday objects without requiring manual annotation or specialized databases. The prompt is formulated to elicit commonsense physical knowledge while constraining the response format for systematic processing:

```
Provide commonsense knowledge
about the physical dimensions and
orientation of the following objects.
Generate a CSV with columns (object,
length, width, height, orientation)
where dimensions are in meters,
orientation is coded as 0=vertical,
1=horizontal, 2=uncertain. Preserve
the exact object names from the input
list and maintain the same number of
objects.
```

TABLE I: The object mapping and localization results on the TUM-RGBD dataset

Seq.	3D IoU $\uparrow$				Centroid (m) $\downarrow$				Size (m) $\downarrow$				ATE (cm) $\downarrow$				
	EAO	VOOM	Ours	Ours+W	EAO	VOOM	Ours	Ours+W	EAO	VOOM	Ours	Ours+W	EAO	VOOM	Ours	Ours+W	ORB3
fr1	0.125	-	<u>0.184</u>	<b>0.242</b>	0.097	-	<u>0.078</u>	<b>0.077</b>	0.092	-	<u>0.078</u>	<b>0.054</b>	<b>1.4894</b>	-	1.8217	<u>1.7678</u>	1.7676
fr2	0.212	0.226	<u>0.338</u>	<b>0.378</b>	0.170	0.096	<u>0.080</u>	<b>0.062</b>	0.147	<u>0.049</u>	0.055	<b>0.047</b>	1.2878	2.3245	<u>1.1084</u>	<b>1.0952</b>	1.0976
fr3	0.127	0.244	<u>0.305</u>	<b>0.326</b>	0.216	0.064	<u>0.062</u>	<b>0.048</b>	0.094	<u>0.044</u>	0.046	<b>0.041</b>	1.3077	1.8233	<u>1.0740</u>	<b>1.0663</b>	1.0686

TABLE II: The object association results on the TUM-RGBD dataset

Seq.	TP				FP				FN				Total
	E	V	O	W	E	V	O	W	E	V	O	W	
fr1	8	-	<b>13</b>	12	1	-	<b>0</b>	<b>0</b>	7	-	<b>2</b>	3	15
fr2	27	<b>29</b>	23	25	<b>3</b>	17	6	4	2	<b>0</b>	6	4	29
fr3	36	<b>44</b>	40	42	<b>0</b>	38	16	7	11	<b>3</b>	7	5	47

The generated priors are integrated directly into our object-level SLAM pipeline as prior estimations. This information serves as soft constraints during optimization, helping to improve initial object pose estimates and constrain solutions when observations are ambiguous.

#### IV. EXPERIMENT

We evaluated the performance on two real-world RGB-D datasets for indoor scenes. Our full object SLAM system was tested on the TUM RGB-D dataset [27]. We validated the effectiveness of our LLM-enhanced priors for online updates on 3RScan [28]. Furthermore, we conducted an ablation study to discuss how each prior affects the mapping results.

##### A. TUM RGB-D

**Dataset** TUM RGB-D dataset is a well-known indoor SLAM benchmark with the ground-truth trajectory provided for test and evaluation. We tested three sequences in the TUM RGB-D dataset under the ‘‘Handheld SLAM’’ category: *freiburg1\_desk* (fr1), *freiburg2\_desk* (fr2), and *freiburg3\_long\_office\_household* (fr3), which are office scenes with cluttered objects.

**Experiment setting** We adopted ORB-SLAM3 [29] to provide the visual odometry, YOLO-v8 [22] as the object detector, and the SORT algorithm for short-time tracking. Since the TUM RGB-D dataset does not provide the ground-truth object location and pose, we manually labeled the objects that could be detected by the YOLO-v8 detector, where labelCloud [30] is the 3D object annotation tool we used here.

We compared our SLAM algorithm with EAO-SLAM and VOOM. Same object detection model was used to ensure a fair comparison. We selected YOLOv8x-seg model since VOOM requires an object detector with segmentation. We also tested our object SLAM with the open-vocabulary YOLO-World detector [31] by feeding a list of common indoor objects as the vocabulary, demonstrating the strength of our LLM-enhanced priors when accurate object category labels are available.

**Evaluation metrics** We found that there is an absence of evaluation metrics for semantic mapping in previous research [8], [10], while we conducted quantitative analysis using our annotated 3D object bounding boxes. We evaluate

the mapping quality by comparing the size and centroid location of the ellipsoid landmarks with the labeled object instances. The centroid error of a landmark is calculated by the Euclidean distance between the estimated quadric centroid and the corresponding centroid of the labeled 3D bounding box. Similarly, we define the size error as the  $L_2$ -norm of difference in quadric size. We also calculated 3D bounding-box IoU using [32] for oriented 3D boxes. We compared how the 3D IoU error performance varies over time, where IoU error is simply  $1 - \text{IoU}$ . The mapping results were evaluated for the estimated objects that are correctly associated. In all of the tables that involve object mapping evaluation, the above three metrics are denoted as ‘‘Centroid’’, ‘‘Size’’, and ‘‘3D IoU’’ respectively.

Although the main contribution here is not about improving object-level data association, it is important to notice that data association and mapping are tightly coupled. Data association can be compromised if object mapping from the first few observations is unsatisfactory, while poor data association also leads to fewer observations per object, which can severely affect the final object mapping quantity. Different from the data-association evaluation in most of the previous research, which only counts the total number of objects that are mapped [10], [13], we conducted a more comprehensive evaluation that differentiates the True Positive (TP), False Positive (FP), and False Negative (FN) – metrics that are often used in the 2D data-association research. TP ensures a one-to-one association between the estimates and ground-truth data. FP refers to the estimated objects that are not in the ground-truth data, and FN counts the number of ground-truth objects which are absent in the estimated map.

We compare the Absolute Trajectory Error (ATE) of the estimated camera trajectory against the provided ground-truth poses. Since we adopt ORB-SLAM3 as the source of visual odometry, the ATE from ORB-SLAM3 (represented by ‘‘ORB3’’) is also calculated as a reference. We also assess the real-time performance of our object SLAM system by the average frame rate, and the breakdown timing on odometry, detection, association, and incremental optimization.

**Results** Table I demonstrates our object mapping results compared to EAO-SLAM and VOOM. The entries ‘‘EAO’’, ‘‘VOOM’’, and ‘‘Ours’’ refer to using EAO-SLAM, VOOM, and our object SLAM method with YOLOv8x-seg detection model correspondingly, and ‘‘Ours+W’’ used our SLAM system with YOLO-World detector. With YOLO-World detector, our SLAM system outperforms other baselines on mapping results across all scenes and achieved the lowest ATE on *fr2* and *fr3* sequences. Since *fr1* has few object

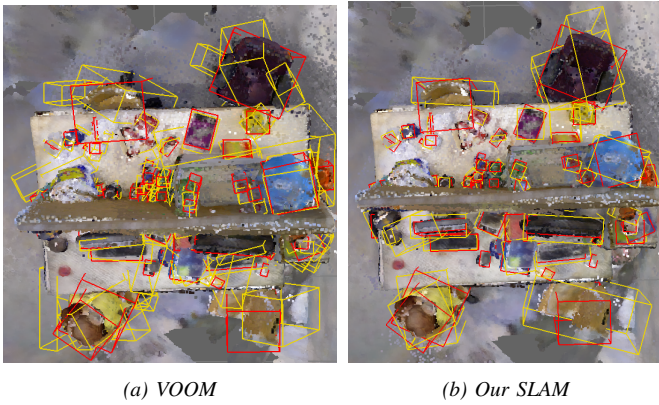


Fig. 4: The quantitative object mapping results on *fr3\_office* using VOOM and our SLAM method. Quadratics are converted to cubes (yellow) to compare with labeled ground-truth objects (red).

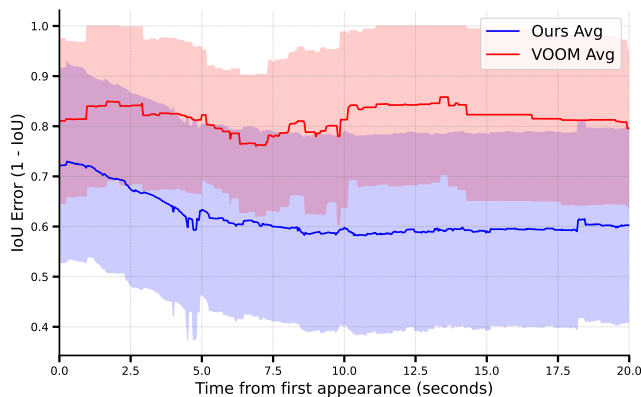


Fig. 5: Average 3D IoU error comparison between VOOM and our SLAM. Background colors of red and blue indicate the standard deviation of IoU error among overlapping objects for each method, where the purple area is simply the overlapping. The experiment was conducted on *fr2\_desk* with YOLOv8x-seg detector.

observations, EAO-SLAM has the advantage of using line detection and dense visual feature. Our SLAM is purely based on ORB-SLAM3 odometry and sparse object-level feature, yet we achieved a similar ATE performance compared with ORB-SLAM3.

We underscored the second best performance in Table I so that we can compare among the SLAM performance using YOLOv8x-seg detection. Under the same detector setting, our SLAM still exceeds the baselines on most of the metrics and sequences. We demonstrate an average of 36.8% increase in 3D IoU compared to VOOM and 78.2% compared to EAO-SLAM. VOOM achieves 7.9% less in size error, but sacrifices in all other metrics by a large margin.

Table II shows the data association results. “Total” refers to the total count of labeled ground-truth (GT) objects. E, V, O, and W are short for EAO-SLAM, VOOM, Ours, and “Ours+W”. EAO-SLAM tends to aggressively associate the object observations and merge multiple objects into one, consequently having a lot of FN results. Conversely, VOOM has a poor data associator. Although VOOM covers the most GT objects, it generates abundant FP objects as well. Fig. 4 is a direct comparison between VOOM’s and our final

TABLE III: The experiment results on the 3RScan dataset

	Online Update		Batch Optimization	
	w/o priors	Ours	w/o priors	Ours
3D IoU $\uparrow$	0.320	<b>0.430</b>	0.400	<b>0.423</b>
Centroid (m) $\downarrow$	0.223	<b>0.090</b>	0.148	<b>0.086</b>
Size (m) $\downarrow$	0.318	<b>0.095</b>	0.196	<b>0.094</b>

object map. Our object map is cleaner and mostly reflects the ground-truth objects.

We calculated the average IoU error among 10 selected objects that have the most correctly associated 2D features for both VOOM and our SLAM. The IoU error comparison is demonstrated in Fig. 5. Our method has better initialization results, and the IoU error decreases faster. With extra constraints from prior factors, our SLAM also exhibits a more consistent descent in IoU error than the trend of VOOM, where the latter method is more vulnerable to poor bounding box observations. During the first 10 seconds from the initial observation of a certain object, the 3D IoU error of our SLAM decreases by 17.1 % and remains similar afterward.

We evaluated the runtime performance of our algorithm on a Laptop with an Intel Core i9 CPU and an Nvidia GeForce GTX 3080 GPU (GPU is only required for YOLOv8 detection. All the other calculations are on CPU). On average, visual odometry requires 18 ms per frame, the object detector takes 24 ms, data association needs 7 ms, and factor graph optimization costs 16.5 ms. The processing speed decreases as more observations are added to the factor graph, dropping from 20 Hz to 2.5 Hz. The overall speed of the online SLAM system averages around 10 Hz on *fr3* sequence.

## B. 3RScan

**Dataset** The 3RScan dataset consists of 1482 scans across 478 different scenes. Each scene was recorded by a handheld Google Tango cellphone, yielding sequences of RGB-D images with calibrated camera poses. 3RScan includes 3D reconstruction of object segmentation, allowing quantitative evaluation of our mapping performance.

**Experiment setting** On the 3RScan dataset, we experimented on 57 scans, which were selected considering feature quantity and diversity. The 3RScan dataset is designed for 3D scene reconstruction and assumes camera odometry has been resolved. The consecutive frames are sampled sparsely, and it is challenging to track the visual features to extract the trajectory or maintain object-level association. We evaluated the mapping results from incremental update of our SLAM algorithm using ground-truth odometry and data association to demonstrate the effectiveness of using priors.

We compared our full SLAM system with the setting under no prior factors and centroid measurements (referred as “w/o priors” in Table III). While the focus is on improving real-time performance, we also compared our algorithm against the same “w/o priors” setting using batch optimization.

**Evaluation metrics** We use the same evaluation metrics for object mapping as in Section IV-A.

**Results** Table III presents our experimental results on the 3RScan dataset, demonstrating that our prior-assisted method

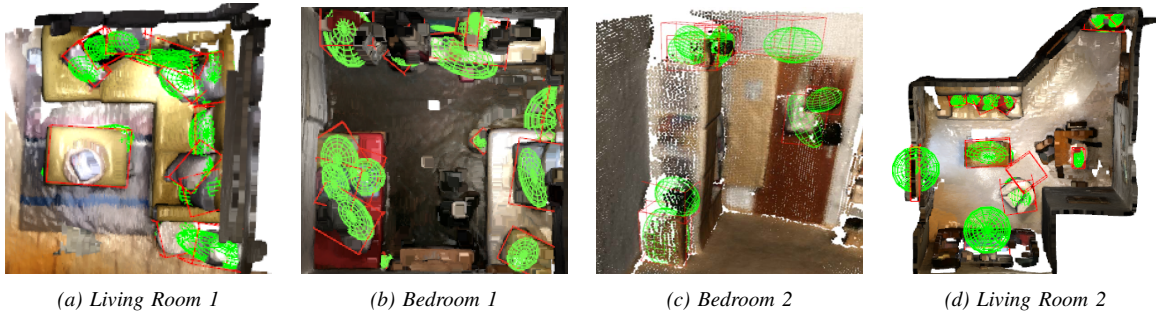


Fig. 6: The final object mapping results on the 3RScan dataset. The ellipsoids (green) represent the estimated object landmarks, and the cubes (red) are the object 3D bounding boxes from point cloud segmentation. Note that there are some bounding boxes without associated point cloud showing in the figure. These are objects located on the ceiling, and we cropped the point cloud for the ceiling to have a better visualization effect.

outperforms no-prior system across all metrics. For online updates, our method reduces object centroid error by 59.6% and object size error by 70.1% compared to the no-prior case. Additionally, our approach achieves higher 3D IoU. Besides, our online method still shows superior performance when compared against no-prior method using batch optimization, with 41.9% lower in centroid error and 52.0% lower in size error. These results validate the effectiveness of our prior factors.

Fig. 6 demonstrates the result of the final maps using online updates for qualitative analysis. Most of the estimated objects are consistent with the segmented instances. There are some objects on the ceilings in Fig. 6c and Fig. 6d that were mapped with displacement compared to the bounding boxes from 3D segmentation. These instances are partially observable and only appear in very few camera frames, and thus it is difficult for the algorithm to initialize and optimize their positions accurately.

### C. Evaluation of LLM-Generated Object Priors

To assess the quality of object priors generated by LLMs, we evaluated the dimensional and rotational accuracy across objects from the TUM RGB-D dataset (27 object types) and 3RScan (222 object types) by comparing with the human-labeled objects. 3RScan dataset provided object annotations, which we found thin objects like papers or notebooks often appear thicker than their actual dimensions for better visualization effects. We manually labeled the objects in the TUM RGB-D dataset on the dense 3D reconstructed scene for each sequence, where a few objects also appear larger than actual object dimensions because of the noise in reconstructed point clouds.

We computed the Mean Relative Error (MRE) between LLM-predicted dimensions and ground truth measurements, finding an average error of 35.2% and 30.8% for 3RScan and TUM RGB-D, respectively. With further analysis by grouping in categories of 3RScan objects, we found that furniture has the lowest MRE of 24.5%, while decorative and stationary objects have the highest MRE of 64.7%. Additionally, 77.5% of objects have a larger labeled volume than the LLM-predicted one, which validates our observation on the labeled objects tend to appear larger and suggests that the labeling inaccuracy partially contributes to the MRE

TABLE IV: Ablation study of LLM-enhanced prior factors on the TUM-RGBD dataset

Seq.	3D IoU $\uparrow$				Centroid (m) $\downarrow$				Size (m) $\downarrow$			
	N	O	S	F	N	O	S	F	N	O	S	F
fr2	.275	.316	.292	<b>.378</b>	.109	.129	.086	<b>.062</b>	.073	.081	.063	<b>.047</b>
fr3	.235	.257	.234	<b>.326</b>	.069	.064	.068	<b>.048</b>	.080	.081	.080	<b>.041</b>

as well. Nevertheless, mechanisms are designed for our LLM-enhanced priors to handle mismatches between LLM-generated sizes and the observations (Section III-B.1).

For orientation classification (vertical, horizontal, or uncertain), we used both strict and weighted metrics. Strict accuracy requiring exact matches reached 66.7% (TUM) and 64.8% (3RScan). Our weighted metric, assigning partial credit (0.5) when either ground truth or prediction is “uncertain,” yielded improved accuracies of 77.8% (TUM) and 68.9% (3RScan), indicating that many predictions are reasonable approximations despite not being exact matches.

### D. Ablation study of prior factors

We conducted an ablation study on the effectiveness of having only one of the prior factors in the object SLAM system. The test was conducted on *fr2\_desk* and *fr3\_office* sequences because these sequences contain the most number of objects among the TUM RGB-D sequences. YOLO-World detector is selected here to demonstrate the best usage of our prior factors.

Table IV presents the results of our ablation study using the same object mapping metrics as in Section IV-A. N, O, S, and F represent respectively the cases when *neither* of the prior factors are deployed, *orientation* prior is used but size prior is eliminated, *size* prior is adopted but orientation prior is missing, and *full* object SLAM system with both priors, which is under the same setting as Ours+W in Table I.

Table IV shows that orientation prior is effective for achieving higher 3D IoU, but may compromise the accuracy in object centroid and size, such as the results in *fr2*. We conjecture that the optimizer attempts to fit quadratics into the bounding box observations with a certain orientation, and even if that causes vastly expanding the ellipsoid size along the camera depth direction. We also found that the object mapping results on *fr3* are similar when one or both prior factors are missing. This is because the incremental optimization solver sometimes lacks enough constraints to

perform online updates when there are not enough prior estimations, leading the final object maps to remain similar to their initialization results. Hence, it is crucial to deploy both prior factors together for the best performance of our object SLAM system.

## V. CONCLUSION

In conclusion, we proposed a real-time object SLAM framework incorporating LLM-inspired prior knowledge as constraints for online factor graph optimization. We demonstrated that our algorithm operates effectively in real-time and real-world scenarios. Using prior factors enhances object-level SLAM results, and analysis showed that LLM-generated priors align well with real-world data.

In future work, we will also explore more in-depth the fusion of image detection methods and point cloud-based methods regarding different categories of objects. Also, data association can achieve greater robustness through scene-level matching in addition to matching at the object level. We also plan to integrate the spatial relationships into a scene graph to establish a more comprehensive understanding. We will ultimately integrate our SLAM with the object search method for the online object-goal navigation task.

## REFERENCES

- [1] Y. Wu, Y. Zhang, D. Zhu, Z. Deng, W. Sun, X. Chen, and J. Zhang, "An object slam framework for association, mapping, and high-level tasks," *IEEE Transactions on Robotics*, vol. 39, no. 4, pp. 2912–2932, 2023.
- [2] H. Zhou, Z. Hu, S. Liu, and S. Khan, "Efficient 2d graph slam for sparse sensing," *arXiv preprint arXiv:2312.02353*, 2023.
- [3] N. Jablonsky, M. Milford, and N. Sünderhauf, "An orientation factor for object-oriented slam," *arXiv preprint arXiv:1809.06977*, 2018.
- [4] W. Ge, C. Tang, and H. Zhang, "Commonsense scene graph-based target localization for object search," in *2024 IEEE/RSJ International Conference on Intelligent Robots and Systems (IROS)*. IEEE, 2024, pp. 13 318–13 325.
- [5] F. Kschischang, B. Frey, and H.-A. Loeliger, "Factor graphs and the sum-product algorithm," *IEEE Transactions on Information Theory*, vol. 47, no. 2, pp. 498–519, 2001.
- [6] M. Hosseinzadeh, K. Li, Y. Latif, and I. Reid, "Real-time monocular object-model aware sparse slam," in *2019 international conference on robotics and automation (ICRA)*. IEEE, 2019, pp. 7123–7129.
- [7] R. F. Salas-Moreno, R. A. Newcombe, H. Strasdat, P. H. Kelly, and A. J. Davison, "Slam++: Simultaneous localisation and mapping at the level of objects," in *Proceedings of the IEEE conference on computer vision and pattern recognition*, 2013, pp. 1352–1359.
- [8] L. Nicholson, M. Milford, and N. Sünderhauf, "Quadricslam: Dual quadrics from object detections as landmarks in object-oriented SLAM," *IEEE Robotics and Automation Letters*, vol. 4, no. 1, pp. 1–8, 2018.
- [9] S. Yang and S. Scherer, "Cubeslam: Monocular 3-d object slam," *IEEE Transactions on Robotics*, vol. 35, no. 4, pp. 925–938, 2019.
- [10] Y. Wu, Y. Zhang, D. Zhu, Y. Feng, S. Coleman, and D. Kerr, "Eao-slam: Monocular semi-dense object slam based on ensemble data association," in *2020 IEEE/RSJ International Conference on Intelligent Robots and Systems (IROS)*. IEEE, 2020, pp. 4966–4973.
- [11] Z. Liao, Y. Hu, J. Zhang, X. Qi, X. Zhang, and W. Wang, "So-slam: Semantic object SLAM with scale proportional and symmetrical texture constraints," *IEEE Robotics and Automation Letters*, vol. 7, no. 2, pp. 4008–4015, 2022.
- [12] Y. Wang, C. Jiang, and X. Chen, "Voom: Robust visual object odometry and mapping using hierarchical landmarks," in *2024 IEEE International Conference on Robotics and Automation (ICRA)*. IEEE, 2024, pp. 10 298–10 304.
- [13] Z. Qian, K. Patath, J. Fu, and J. Xiao, "Semantic slam with autonomous object-level data association," in *2021 IEEE International Conference on Robotics and Automation (ICRA)*. IEEE, 2021, pp. 11 203–11 209.
- [14] M. Zins, G. Simon, and M.-O. Berger, "Oa-slam: Leveraging objects for camera relocalization in visual slam," in *2022 IEEE international symposium on mixed and augmented reality (ISMAR)*. IEEE, 2022, pp. 720–728.
- [15] Y. Fang, K. Kuan, J. Lin, C. Tan, and V. Chandrasekhar, "Object detection meets knowledge graphs," in *Proceedings of the 26th International Joint Conference on Artificial Intelligence*, ser. IJCAI'17. AAAI Press, 2017, p. 1661–1667.
- [16] A. Pal, Y. Qiu, and H. Christensen, "Learning hierarchical relationships for object-goal navigation," in *Conference on Robot Learning*. PMLR, 2021, pp. 517–528.
- [17] M. Hosseinzadeh, Y. Latif, T. Pham, N. Sünderhauf, and I. Reid, "Structure aware SLAM using quadrics and planes," in *Computer Vision—ACCV 2018: 14th Asian Conference on Computer Vision, Perth, Australia, December 2–6, 2018, Revised Selected Papers, Part III 14*. Springer, 2019, pp. 410–426.
- [18] D. Shah, M. R. Equi, B. Osiński, F. Xia, B. Ichter, and S. Levine, "Navigation with large language models: Semantic guesswork as a heuristic for planning," in *Conference on Robot Learning*. PMLR, 2023, pp. 2683–2699.
- [19] Z. Zhao, W. S. Lee, and D. Hsu, "Large language models as common-sense knowledge for large-scale task planning," *Advances in Neural Information Processing Systems*, vol. 36, pp. 31 967–31 987, 2023.
- [20] J. Yang, S. Yang, A. W. Gupta, R. Han, L. Fei-Fei, and S. Xie, "Thinking in space: How multimodal large language models see, remember, and recall spaces," *arXiv preprint arXiv:2412.14171*, 2024.
- [21] M. Kaess, H. Johannsson, R. Roberts, V. Ila, J. J. Leonard, and F. Dellaert, "iSAM2: Incremental smoothing and mapping using the bayes tree," *The International Journal of Robotics Research*, vol. 31, no. 2, pp. 216–235, 2012.
- [22] G. Jocher, A. Chaurasia, and J. Qiu, "Ultralytics yolo," Jan. 2023, version 8.0.0, AGPL-3.0 license. [Online]. Available: <https://github.com/ultralytics/ultralytics>
- [23] N. Wojke, A. Bewley, and D. Paulus, "Simple online and realtime tracking with a deep association metric," in *2017 IEEE International Conference on Image Processing (ICIP)*, 2017, pp. 3645–3649.
- [24] —, "Simple online and realtime tracking with a deep association metric," in *2017 IEEE International Conference on Image Processing (ICIP)*, 2017, pp. 3645–3649.
- [25] N. Aharon, R. Orfaig, and B.-Z. Bobrovsky, "BoT-SORT: Robust associations multi-pedestrian tracking," 2022.
- [26] J. Pennington, R. Socher, and C. D. Manning, "Glove: Global vectors for word representation," in *Empirical Methods in Natural Language Processing (EMNLP)*, 2014, pp. 1532–1543. [Online]. Available: <http://www.aclweb.org/anthology/D14-1162>
- [27] J. Sturm, N. Engelhard, F. Endres, W. Burgard, and D. Cremers, "A benchmark for the evaluation of RGB-D SLAM systems," in *2012 IEEE/RSJ International Conference on Intelligent Robots and Systems*, 2012, pp. 573–580.
- [28] J. Wald, A. Avetisyan, N. Navab, F. Tombari, and M. Niessner, "RIO: 3D Object Instance Re-Localization in Changing Indoor Environments," in *Proceedings IEEE International Conference on Computer Vision (ICCV)*, 2019.
- [29] C. Campos, R. Elvira, J. J. G. Rodriguez, J. M. M. Montiel, and J. D. Tardos, "ORB-SLAM3: An accurate open-source library for visual, visual-inertial, and multimap SLAM," *IEEE Transactions on Robotics*, vol. 37, no. 6, p. 1874–1890, Dec. 2021. [Online]. Available: <http://dx.doi.org/10.1109/TRO.2021.3075644>
- [30] C. Sager, P. Zschech, and N. Kühl, "labelcloud: A lightweight domain-independent labeling tool for 3d object detection in point clouds," 2021.
- [31] T. Cheng, L. Song, Y. Ge, W. Liu, X. Wang, and Y. Shan, "Yolo-world: Real-time open-vocabulary object detection," in *Proc. IEEE Conf. Computer Vision and Pattern Recognition (CVPR)*, 2024.
- [32] N. Ravi, J. Reizenstein, D. Novotny, T. Gordon, W.-Y. Lo, J. Johnson, and G. Gkioxari, "Accelerating 3d deep learning with pytorch3d," *arXiv:2007.08501*, 2020.